A Practical Precision Control Method Base on Linear Extended State Observer and Friction Feedforward of Permanent Magnet Linear Synchronous Motor

XIUFENG LIU [1,2], **HAIYIN CAO** [1,2], **WEI WEI** [2], **JINZHOU WU** [1,2], **BO LI** [3], **AND YU HUANG** [1]

[1] State Key Laboratory of Digital Manufacturing Equipment and Technology, School of Mechanical Science and Engineering, Huazhong University of Science and Technology, Wuhan 430074, China
[2] Institute of Machinery Manufacturing Technology, China Academy of Engineering Physics, Chengdu 610200, China
[3] School of Mechanical Engineering, Hubei University of Arts and Science, Xiangyang 441053, China

Corresponding author: Yu Huang (yuhuang_hust@hust.edu.cn)

ABSTRACT In this paper, a detailed model of motion stage driven by iron-less permanent magnet linear synchronous motor (PMLSM) and supported by rolling guides are presented. This stage is a prototype of the feeding system for a precise turning machine tool. In this model, there are two categories disturbances including slow-varying ones mainly produced by the thrust ripple of PMLSM and abrupt-changing ones caused by nonlinear friction of rolling guide. To overcome these disturbances, a simple, effective and practical servo control method based the general-purpose two-degree-of-freedom PID (2DoF-PID) type controller integrated with the linear extended state observer (LESO) and the friction feedforward (FFF) controller is presented. In this control framework, the linear ESO is designed to estimate and compensate for the slow-varying disturbance and the FFF controller is adopted to eliminate the abrupt-changing nonlinear friction effects. Finally, comparative simulations indicate that the 2DoF-PID-LESO-FFF is effective and achieves better performance compared with traditional controllers, and experiment results demonstrate that the tracking error of the proposed method can be kept in the bounds of 1.5 μm under different conditions.

I. INTRODUCTION

In recent years, permanent magnet linear synchronous motor (PMLSM), which has some excellent features such as super-power density, high speed and acceleration, low thermal losses, and long service life, has been widely used in a high-performance automatic control system, such as chip fabrication equipment, optical measuring instrument, and ultra-precision CNC machine tool. Compared with conventional rotary PMSM with ball-screw as a linear feeding system, PMLSM drive motion system without any intermediate transmission is more suitable for high speed, high precise, and rapid dynamic response application [1]. Meanwhile, the motion control of the PMLSM servo system has to directly

The associate editor coordinating the review of this manuscript and approving it for publication was Nasim Ullah [ID].

confront the adverse effects caused by various undesirable disturbances.

This paper's research object is a positioning stage, which is driven by an iron-less PMLSM and supported by a set of rolling guides, and its schematic diagram is shown in Fig. 1. In this stage, the disturbances can be roughly divided into external and internal. The external ones mainly come from nonlinear dynamic friction, viscous resistance, nominal working load and inevitable mechanical vibration during machine operation [2]. The internal ones are mainly caused by end effects, cogging force, the variation of motor parameters (i.e., the resistance, the inductance, and the flux linkage, etc.), offset and quantization error of signal conversion modules (i.e., current sensors, D/A and A/D converters) [3]. It is very worth noting that thrust ripple caused by the end and cogging effects can be approximately simplified
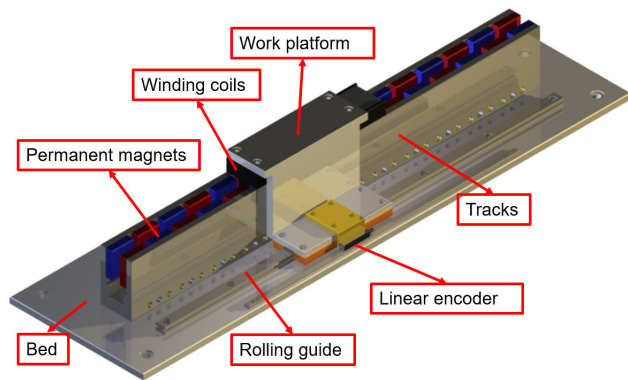
FIGURE 1. Schematic diagram of the motion stage structure.

into a sinusoidal function [4]. The periodicity of the above function is only relevant to the position of winding coil, and the amplitude is determined by both mover position and current of the stator along the q axes(i_q). Trust ripple will reduce the stability of servo control systems, making it easy to occur velocity oscillation at low-speed movement [5]. Velocity oscillation will not only seriously deteriorate the positioning performance of servo systems, but also may cause additional vibration of the machine. In particular, when the fluctuation frequency happens to be close to or consistent with the natural frequency of the equipment, the resulting vibration will greatly reduce the accuracy of the equipment.

Technologies for improving the PMLSM performance in high speed and precision applications have been constantly studied in recent decades. The ongoing research results can be roughly classified into optimization designs of a linear motor and adopting appropriate control algorithms.

The main idea of magnetic and mechanical optimal design is to modify the size and shape of permanent magnets (PMs), winding coils, and teeth-slots. Inoue and Sato presented methods to calculate the best coil length by Finite Element Method (FEM) calculations [6]. Lee *et al.* proposed methods to design PM length, PM group shifting length, and slot opening length by the combination of finite element analysis (FEA) and response surface method (RSM) [7]. Zhu *et al.* proposed to employ semi-closed slots and auxiliary poles to reduce detent force [8], [9]. Wang *et al.* performed methods to design skewed PMs which can reduce the high order harmonic components thrust ripple [1]. In general, the optimizing structure of PMLSM, without doubt, will increase the complexity of motor construction and the total cost of equipment. Moreover, the improvement effectiveness of these optimal methods is limited.

To compensate for the adverse influences of total disturbances on the PMLSM stage, recently researchers have produced numerous control algorithms. PID control strategy is still a mature and widely used control framework. Therefore, many scholars integrated PID with a general-purpose feedforward controller and based model compensator in PMLSM applications. Zhao *et al.* used adaptive

feedforward control compensation to eliminate the impact of thrust fluctuation of linear motor [10]. Yan *et al.* proposed a combined two-degree-of-freedom (2DoF) controller and disturbance observer (DOB) method to control the linear motor in EDM machines [11], [12]. Bascetta *et al.* identified the force ripple model of the linear motor by a frequency-domain method and performed direct compensation [13]. Xi *et al.* presented a compensation method for ultra-low-velocity feeding, which is based on an accurate model of iron-less PMLSM stage [14].

Based on the abovementioned methods, it can be found that the disturbance observer (DOB) is an intuitive and effective method to compensate for the thrust ripple of a linear motor. However, in the process of the actual application, there is an inevitable problem that the effectiveness of the DOB compensator depends on the accuracy of the system model, but a time-invariant system is essentially unrealizable. Therefore, some improvements are proposed, and the core idea is that using an observer possessed a certain adaptive ability to compensate for the dynamic model parameter errors between nominal and actual. Zhang *et al.* proposed a neural network feedforward based on the BP algorithm for suppressing the force ripple in a precision motion stage [15]. Wang *et al.* combined the feedback of predictive function control (PFC) and the feedforward of extended state observer (ESO) to improve the speed tracking performance [16]. Jin *et al.* presented a feedforward method based on a 7th-order extended Kalman filter to achieve disturbance compensation [17]. Yang *et al.* focused on the thrust ripple of PMLSM estimation and compensation with a novel incremental extended state modeling-based Kalman filter (IESM-KF) [18].

In addition, the repetitive control (RC) and iterative learning control (ILC) achieve a favorable effect in the field of robotic arms and semiconductor fabrication equipment. Some researchers introduced the RC and ILC methods into the DOB to eliminate the periodical disturbances for PMLSM. Chen *et al.* used a repetitive controller into a gantry type machine tool [19]. Luo *et al.* proposed a dual high-order periodic adaptive learning compensation (DHO-PALC) to minimize the cogging effects treated as position-dependent periodic disturbance [20]. Cho *et al.* proposed an effective periodical adaptive disturbance observer for the PMLSM stage working in the periodic and repetitive condition [21], [22]. Zhang *et al.* combined a model reference adaptive controller (MRAC) and periodic adaptive learning controller (PALC) to control the PMLSM stage working under repetitive motion tasks [23]. Fu *et al.* integrated inverse model iterative learning control (IMILC) into robust DOB to compensate thrust ripple of linear motor [24].

Furthermore, robust control methods maintain good performance under certain parameter perturbations. The idea of sliding mode control (SMC), which is one of the most widely used robust control methods in PMSM servo control, has been extended to PMLSM. Cheema *et al.* proposed a combined speed and direct thrust force control (DTFC) scheme based on SMC [25]. Yang *et al.* utilized a predictive current
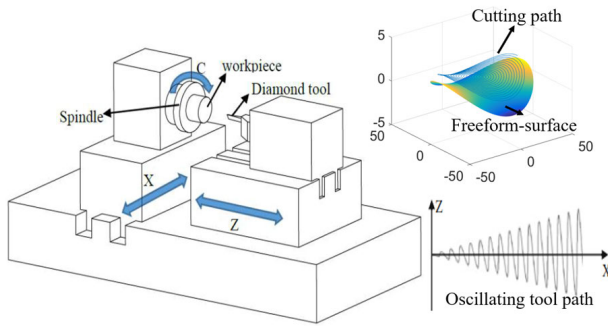
FIGURE 2. Schematic of STS turning for free-form surfaces.

controller (PCC) to achieve current loop control and second order sliding mode observer (SOSMO) based on a super-twisting algorithm was integrated into PCC for compensating the parameter mismatch [3]. Zhao *et al.* illustrated an adaptive terminal sliding mode controller based on RBF neural network to estimate and compensate the unmodeled disturbances in PMLSM servo system [26]. Jiang *et al.* presented a smooth sliding mode controller for PMSLM speed control [27].

Remarkably, the motion stage studied in this paper is a prototype of the feeding system for a micro-precision turning machine tool. Single-point diamond turning is well-known to be the most effective in fabricating precision surfaces [28]. And with the introduction of the Fast-Tool-Servo (FTS) and Slow-Tool-Servo (STS) processing technics, non-rotationally symmetric surfaces can also be machined by the diamond turning machine. Fig. 2 illustrated a machining example of a slow tool servo for off-axis aspheric mirrors. The workpiece is mounted on the center of the spindle, the spindle moves along the X-axis under constant velocity, and the diamond tool oscillates along the Z-axis [29]. The linear X- and Z-axes and the spindle C-axis under fully coordinated position control to form the machined surfaces. The machined surface quality (geometrical accuracy) is directly based on the performance of tracking of the motion trajectory. Therefore, the servo control target is that the maximum tracking error is no more than 1.5 μm in a constant velocity movement and no more than 3 μm in a reasonable frequency and amplitude sinusoidal reference signal.

In the STS machining, the Z-axis is usually required to execute reciprocating movement according to the processing surface shape. The nonlinear friction, in the rolling guides, degrades tracking accuracy of moving axes, especially at velocity reversals. Hence, to overcome this problem and to achieve high performance of servo control systems, an appropriate friction model that describes friction characteristics is required. Xi *et al.* proposed a two-stage friction compensation scheme based on the classical Karnopp model for the nonlinear friction during the transition from the pre-sliding regime to the sliding regime [30]. Ruderman presented a feedforward friction observer (FFFO) based on the two-state elastoplasticity (2SEP) model [31]. Yang *et al.* proposed a novel two-stage friction model combined static friction model and classical

Tustin model [32]. Sparham *et al.* adopted an adaptive neuro-fuzzy inference system (ANFIS) model to predict the friction forces in CNC guideways [33]. Hazem *et al.* proposed a neuro-fuzzy friction estimation model (NFFEM) to evaluate the joint friction in a triple link rotary inverted pendulum [34].

Aiming at the aforementioned problems of this motion stage, the paper presents an effective and practical control scheme based on the common 2DoF-PID type controller integrated with a linear ESO and a friction feedforward (FFF) controller. The linear ESO, which is first introduced in active disturbance rejection control (ADRC) by Prof. Han [35], can be viewed as an adaptive observer that can estimate and compensate for the slow-varying disturbances including the model parameter errors [36]. The model-based FFF controller is used to eliminate the nonlinear abrupt-change friction in this stage. The remaining parts of this paper are organized as follows: Section.2 introduces the model of PMLSM. Section.3 demonstrates the design of the 2DoF-PID-LESO-FFF method. Section.4 illustrates the experimental setup, system identification, simulation results, and experimental results. Finally, Section.5 concludes this paper.

II. PROBLEM FORMULATION
A. DYNAMIC MODELING OF THE MOTION STAGE
In this section, a model of the three-phase iron-less PMLSM driving a linear positioning stage supported by rolling guides will be presented. Electromechanical model of the stage with loads and disturbances is given by

$$
\begin{aligned}
m\ddot{x}(t) &= F_e - B\dot{x}(t) + d \\
&= K_e i_q(t) - B\dot{x}(t) + d \quad (1)
\end{aligned}
$$

where $x(t)$ is the mover position, m is the total mass of the moving part, F_e is the electromagnetic force, B is the viscous friction coefficient of linear guide, K_e is the thrust coefficient of PMLSM, i_q is the current of the stator along the q axes, d is the lumped force disturbance which can be simply described as

$$
d = F_{rip} + F_{fric} + F_L \quad (2)
$$

where F_{rip} is the inherent force ripple, F_{fric} is the nonlinear friction force, F_L is the nominal working load and other unmodeled force. Iron-less PMLSM has an important extra advantage of no cogging force fluctuation compared to iron-core PMLSM [14]. In this paper, the thrust ripple is produced only by the end effects, which can be described as

$$
F_{rip} = A_r sin\left(\frac{2\pi}{\tau_p}x + \varphi_n\right) i_q^2(t) \quad (3)
$$

where A_r is the coefficient of end effects, τ_p is the N-S poles pitch of linear motor, φ_n is an initial phase parameter. The motor in the platform is supported by linear rolling guides, therefore, it is necessary to consider the nonlinear friction which may be modeled as a combination of Coulomb friction
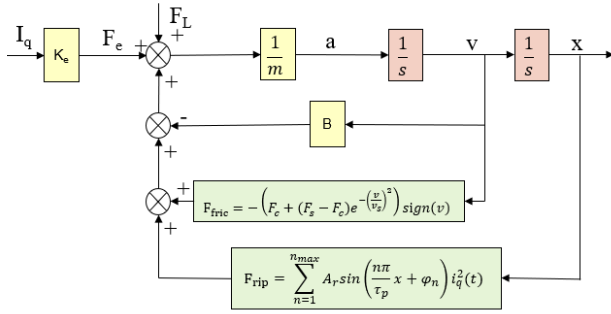
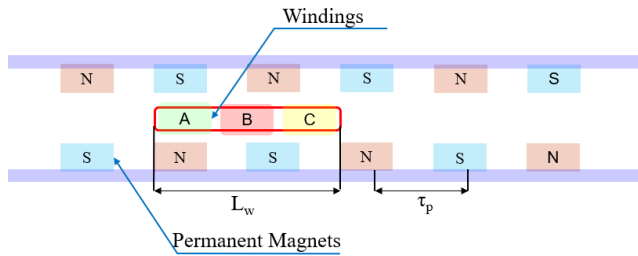**FIGURE 3.** Block diagram of PMLSM positioning stage.

FIGURE 4. Top view of iron-less PMLSM structure.

and the component due to Stribeck effects

$$F_{fric} = -\left(F_c + (F_s - F_c)\, e^{-\left(\frac{v}{v_s}\right)^2}\right) sign\,(v) \qquad (4)$$

where F_c is the Coulomb friction force, F_s is the maximum static friction force, v_s is the Stribeck velocity, v is the mover velocity. According to Eqs. (1), (2), (3) and (4), the block diagram of the linear motor positioning stage is illustrated in Fig. 3.

B. MODELING AND ANALYSIS OF THE IRON-LESS PMLSM THRUST RIPPLE

Fig. 4 illustrates the structure diagram of iron-less PMLSM. The permanent magnets are evenly distributed on both sides of the U-shaped inner slot, and the N-S pole pitch is τ_p. The mover of linear motor consists of ABC three-phase winding coils, and the length of one group of ABC winding coils is L_w. To analyze thrust ripple caused by end effects, some reasonable hypotheses are assumed as follows:

1) PMs are magnetized uniformed, and the distribution of the air gap magnetic field is considered as a sinusoidal wave.

2) The electrical characteristics of three-phase winding coils are identical, and $L_w = 2\tau_p$.

3) Neglecting the effects of the magnetic flux distortions and saturations.

The thrust force of the linear motor is generated by the magnetic flux linkage and the winding coils current as follow

$$F_e = p_n[\vec{\Psi}_s \times \vec{I}_s] \qquad (5)$$

where F_e is the total output thrust force, p_n is the group number of winding coils, $\vec{\Psi}_s$ is the total flux linkage, $\vec{I}_s$ is the winding current. The total flux linkage is composed of two

parts: one is generated by the permanent magnets, the other is energized by the winding current themselves as follow

$$\vec{\Psi}_s = \vec{\Psi}_f + \vec{\Psi}_w \qquad (6)$$

where $\vec{\Psi}_f$ is the flux linkage generated by the permanent magnets, $\vec{\Psi}_w$ is the flux linkage energized by the winding current.

As is well known, a permanent magnet can be thought of as an electrified coil. To simplify the discussion, adopting equivalent mutual inductance and equivalent magnetizing current to simulate motor PMs excitation flux linkage, which can be expressed as follow

$$\vec{\Psi}_f = \vec{L}_f \cdot i_f \qquad (7)$$

$$\vec{L}_f = \begin{bmatrix} M_{fA} \\ M_{fB} \\ M_{fC} \end{bmatrix} = \begin{bmatrix} M_{AM}\cos(\theta_e) \\ M_{BM}\cos\left(\theta_e - \frac{2\pi}{3}\right) \\ M_{CM}\cos\left(\theta_e + \frac{2\pi}{3}\right) \end{bmatrix} \qquad (8)$$

$$\theta_e = \frac{\pi}{\tau_p}x \qquad (9)$$

where $\vec{L}_f$ is equivalent mutual-inductance vector, i_f is equivalent magnetizing current. The mutual inductance of simulated coils and winding coils can be written as M_{fA}, M_{fB}, and M_{fC}. Since the above assumption that the distribution of the magnetic field is a sinusoidal wave, it is obvious that M_{fA}, M_{fB}, and M_{fC} are sinusoidal functions of the position. M_{AM}, M_{BM}, and M_{CM} are the maximum mutual inductances, θ_e is the phase angle of the A-phase winding coil position, x is the position of A-phase winding coil. Meanwhile, since the above assumption that the length of a group of winding coils is exactly twice the N-S pole pitch, the phase difference of any two adjacent coils is 120 degrees.

The flux linkage generated by the motor internal winding coils can be divided into two categories: self-inductances and mutual-inductances.

$$\vec{\Psi}_w = \boldsymbol{L}_{ABC}\vec{I}_s = \begin{bmatrix} L_A & M_{AB} & M_{AC} \\ M_{BA} & L_B & M_{BC} \\ M_{CA} & M_{CB} & L_C \end{bmatrix}\begin{bmatrix} i_A \\ i_B \\ i_C \end{bmatrix} \qquad (10)$$

where $\boldsymbol{L}_{ABC}$ is the coefficient matrix of three-phase motor winding inductances, L_A, L_B, and L_C are the three-phase winding current self-inductance coefficients, M_{AB}, M_{BA}, M_{BC}, M_{CB}, M_{AC}, and M_{CA} are three-phase winding current mutual-inductance coefficients, I_s is three-phase winding current vector, i_A, i_B, and i_C are the three-phase winding currents.

To facilitate theoretical analysis and decoupling control, the $d-q$ coordinate system has been widely used in the motor control field. The Clark and Park transformation accomplish the coordinate transformation from ABC coordinate to d-q coordinate. $\boldsymbol{K}_{3s/2r}$ is Clark and Park transformational matrix, and $\boldsymbol{K}_{2r/3s}$ is the inverse matrix of $\boldsymbol{K}_{3s/2r}$.

$$\boldsymbol{K}_{3s/2r} = \sqrt{\frac{2}{3}}\begin{bmatrix} cos\theta_e & \cos\left(\theta_e - \frac{2\pi}{3}\right) & \cos\left(\theta_e + \frac{2\pi}{3}\right) \\ -sin\theta_e & -\sin\left(\theta_e - \frac{2\pi}{3}\right) & -\sin\left(\theta_e + \frac{2\pi}{3}\right) \end{bmatrix} \qquad (11)$$

$$\boldsymbol{K}_{2r/3s} = \sqrt{\frac{2}{3}}\begin{bmatrix} cos\theta_e & -sin\theta_e \\ \cos\left(\theta_e - \frac{2\pi}{3}\right) & -\sin\left(\theta_e - \frac{2\pi}{3}\right) \\ \cos\left(\theta_e + \frac{2\pi}{3}\right) & -\sin\left(\theta_e + \frac{2\pi}{3}\right) \end{bmatrix} \qquad (12)$$

Eqs. (7), (10), and (6) can be transformed in d-q coordinate system respectively

$$\vec{\Psi}_{f_{dq}} = \mathbf{K}_{3s/2r}\vec{L}_f i_f = \begin{bmatrix} L_{f_1} \\ L_{f_2} \end{bmatrix} i_f \tag{13}$$

$$\vec{\Psi}_{w_{dq}} = \mathbf{K}_{3s/2r}\mathbf{L}_{ABC}\mathbf{K}_{2r/3s}\begin{bmatrix} i_d \\ i_q \end{bmatrix}$$

$$= \begin{bmatrix} L_{s_{11}} & L_{s_{12}} \\ L_{s_{21}} & L_{s_{22}} \end{bmatrix}\begin{bmatrix} i_d \\ i_q \end{bmatrix} \tag{14}$$

$$\vec{\Psi}_{s_{dq}} = \vec{\Psi}_{f_{dq}} + \vec{\Psi}_{w_{dq}} = \begin{bmatrix} L_{f_1}i_f + L_{s_{11}}i_d + L_{s_{12}}i_q \\ L_{f_2}i_f + L_{s_{21}}i_d + L_{s_{22}}i_q \end{bmatrix} \tag{15}$$

where i_d is the current of the stator along the d axes, i_q is the current of the stator along the q axes. Eq. (5) can be derived as

$$F_e = P_n[\vec{\Psi}_s \times \vec{I}_s]$$
$$= P_n\begin{bmatrix} L_{f_1}i_f + L_{s_{11}}i_d + L_{s_{12}}i_q \\ L_{f_2}i_f + L_{s_{21}}i_d + L_{s_{22}}i_q \end{bmatrix} \times \begin{bmatrix} i_d \\ i_q \end{bmatrix} \tag{16}$$

Since the iron-less PMLSM, investigated in this paper, belongs to the surface-mounted permanent motor, $i_d = 0$ is the most common control strategy in this category. Eq. (16) can be directly simplified to

$$F_e = P_n\left(L_{f_1}i_f i_q + L_{s_{12}}i_q^2\right) \tag{17}$$

and L_{f_1} and $L_{s_{12}}$ can be expressed respectively as

$$L_{f_1} = \frac{\sqrt{6}}{8}(2M_{AM} - M_{BM} - M_{CM})\cos2\theta_e$$
$$+ \frac{3\sqrt{3}}{8}(M_{BM} - M_{CM})\sin2\theta_e$$
$$+ \frac{\sqrt{6}}{4}(M_{AM} + M_{BM} + M_{CM}) \tag{18}$$

$$L_{s_{12}} = \frac{\sqrt{6}}{8}(-2L_A + L_B + L_c + M_{AB} + M_{BA}$$
$$+ M_{AC} + M_{CA} - 2M_{BC} - 2M_{CB})\sin2\theta_e$$
$$+ \frac{3\sqrt{2}}{8}(-L_B + L_C + M_{AB}$$
$$+ M_{BA} - M_{AC} - M_{CA})\cos2\theta_e$$
$$+ \frac{3\sqrt{2}}{8}(M_{AB} - M_{BA} + M_{BC}$$
$$- M_{CB} + M_{CA} - M_{AC}) \tag{19}$$

The electrical characteristics of the three-phase winding coils have been assumed to be identical, so the three-phase maximum equivalent mutual-inductances are in the same value ($M_{AM} = M_{BM} = M_{CM} = M_s$), and the three-phase winding current self-inductance are also equal ($L_A = L_B = L_C = L_s$). Since the linear motor in this paper belongs to the type of short moving primary and long stationary secondary, it is evident that the mutual-inductance of A&C coils is quite different from that of A&B and B&C ($M_{AB} = M_{BA} = M_{BC} = M_{CB} = M_{n1}$, $M_{AC} = M_{CA} = M_{n2}$, $M_{n1} \neq M_{n2}$). Eqs. (16), (17), and (18) can be established as

$$F_e = P_n\{\frac{\sqrt{6}}{2}M_s i_f i_q + [\frac{1}{6}(M_{n2} - M_{n1})\cos(2\theta_e)$$
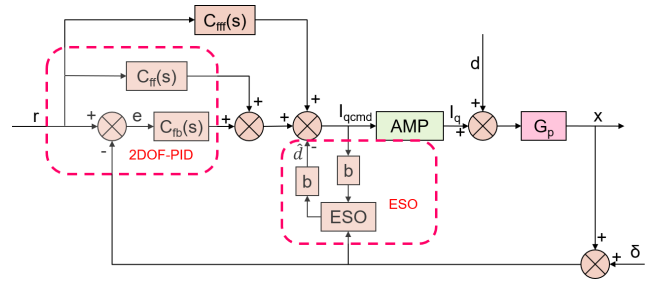$$+ \frac{\sqrt{3}}{6}(M_{n1} - M_{n2})\cos(2\theta_e)]i_q^2\} \tag{20}$$

FIGURE 5. The control structure of the 2DoF-PID-LESO-FFF controller.

According to the Eq. (19), it is obvious that the flux linkage generated by PMs is the main source of output, which is proportional to the current i_q. Meanwhile, for the iron-less PMLSM, the rest of the electromagnetic force derived from coil-magnets is the primary cause of thrust force fluctuation, which brings a certain extent of nonlinear factor into the motion system.

There are two categories of nonlinear factors in the positioning stage driven by iron-less PMLSM and supported by rolling guides. The first category is the nonlinear frictional disturbance, which can be approximated as a saturation function with a high steep curve, in the process of starting, stopping and reciprocating movement. The peculiarity of friction nonlinearity can be regarded as that the change rate is rapid and the intensity is small. The second category comes from the thrust fluctuation caused by the end effect of the linear motor. The nonlinear ripple can be approximated into a sinusoidal function related to the position of the mover. The amplitude of fluctuation can be approximated as proportional to the square of the i_q, and its period is exactly equal to the N-S pole pitch. The characteristic of motor thrust fluctuation can be considered as that the intensity is large and the varying rate is slow.

III. CONTROLLER DESIGN

Compared with the rotary motor with reduction gears and ball screws, the linear motor generates the thrust force directly to loads without the intervention of the mechanical transmission that can be as a buffer. Therefore, in order to handle the platform with large amounts of in both internal electromagnetic interferences and external mechanical disturbances, this section presents a servo control strategy that consists of the conventional 2DoF-PID, linear ESO (LESO) and friction feedforward (FFF) in detail. The main idea is that adopting LESO to observe and compensate for the slow-changing disturbances (i.e., end effects, the change of working loads, etc.) and using a model-based friction feedforward controller to eliminate abrupt-changing interference due to nonlinear friction. Fig.5 shows the block diagram of the 2DoF-PID-LESO-FFF scheme, r is the given reference position, $I_{q_{cmd}}$ is the controller output used to control servo amplifier, I_q is the actual q-axes current of the linear motor, d is the total disturbances of electromechanical system, x is the actual

position, δ is signal noise of position sensor, $\hat{d}$ is the total disturbances estimated by the LESO.

A. LINEAR EXTENDED STATE OBSERVER

The second order differential equation Eq. (1) of linear motor stage can be rewritten as state-space equations

$$\begin{cases} \dot{x}_1 = x_2 \\ \dot{x}_2 = bu - ax_2 + D \end{cases} \tag{21}$$

where x_1 and x_2 are the system states, x_1 represents the actual position, x_2 represents the actual velocity, $a = B/m$ and $b = K_e/m$ are the system parameters, $u = i_q$ is the output of servo amplifier, $D = d/m$ is the unmodeled disturbances. It is worth noting that extended state observer has the ability to estimate the whole disturbances including the interference derived from system parameters mismatch against the nominal value. d_c is the whole disturbances that can be constructed as

$$d_c = (b - b_n) u - (a - a_n) x_2 + D \tag{22}$$

where a_n and b_n are the nominal value which is given by the system identification. The state-space of Eqs. (21) can be extended. In the absence of nonlinear friction, end effects, and other disturbances, the differential formula of Eq. (1) can be rewritten into the second-order transfer function

$$\begin{cases} \dot{x}_1 = x_2 \\ \dot{x}_2 = b_n u - a_n x_2 + x_3 \\ \dot{x}_3 = h(t) \end{cases} \tag{23}$$

where x_3 is the whole disturbances. The linear extended state observer, which is first systematically proposed by Prof. Gao [37], can be expressed as

$$\begin{cases} \dot{\hat{x}}_1 = \hat{x}_2 + \beta_1(x - \hat{x}_1) \\ \dot{\hat{x}}_2 = b_n u - a_n \hat{x}_2 + \hat{x}_3 + \beta_2(x - \hat{x}_1) \\ \dot{\hat{x}}_3 = \beta_3(x - \hat{x}_1) \end{cases} \tag{24}$$

where $\hat{x}_1$, $\hat{x}_2$, and $\hat{x}_3$ are the estimated states of Eq. (23), β_1, β_2, and β_3 are the gains of ESO, Let, $\beta_1 = 3\omega$, $\beta_2 = 3\omega^2$, and $\beta_3 = \omega^3$, where ω is the concept of bandwidth for the linear ESO, and its value is determined by requirements of servo controller. However, Eq. (24) of LESO is hardly applied directly into the servo control algorithm because the analytic solutions for ODEs are difficult to obtain in general. The Eq. (25) can be approximately solved by Euler-method as

$$\begin{cases} \hat{x}_1(k) = \hat{x}_1(k-1) + h\{\hat{x}_2(k-1) + \beta_1[x(k) \\ \qquad - \hat{x}_1(k-1)]\} \\ \hat{x}_2(k) = \hat{x}_2(k-1) + h\{b_n u(k) - a_n \hat{x}_2(k-1) \\ \qquad \hat{x}_3(k-1) + \beta_2[x(k) - \hat{x}_1(k-1)]\} \\ \hat{x}_3(k) = \hat{x}_3(k-1) + h\beta_3[x(k) - \hat{x}_1(k-1)] \end{cases} \tag{25}$$

where h is the step of Euler-method, and its value is the single computing cycle period of the embedded computer. Eq. (25) is the discretized LESO, which is more suitable for a digital servo controller.

B. 2DoF-PID CONTROLLER

In the absence of nonlinear friction, end effects, and other disturbances, the differential formula of Eq. (1) can be rewritten into the second-order transfer function

$$G_p(s) = \frac{X(s)}{I_q(s)} = \frac{K_e}{ms^2 + Bs} \tag{26}$$

The 2DoF-PID control goal is to make the tracking error of the motion system as small as possible while stabilizing the closed-loop control system from the interferences of noise and high-frequency command signals.

Since the low-pass filter has the ability to filter out high-frequency signals, the dynamic response of the feedback-PID controller can be designed as a first-order low-pass filter.

$$Q(s) = \frac{X(s)}{R(s)} = \frac{1}{1 + \tau s} \tag{27}$$

where $Q(s)$ is the first-order filter, τ is the filter time constant, and its value is determined by the requirements of the servo controller. The feedback-PID control system can be designed base on the nominal parameters of the motion system, and its transfer function is expressed as

$$\begin{aligned} C_{fb}(s) &= \frac{X(s)}{R(s) - X(s)} \frac{1}{G_n(s)} \\ &= \frac{1}{\tau s} G_p(s)^{-1} \\ &= \frac{m_n}{K_{en}\tau} s + \frac{B_n}{K_{en}\tau} \end{aligned} \tag{28}$$

where m_n is the nominal total mass of mover, K_{en} is the nominal thrust coefficient of PMLSM, B_n is the nominal viscous friction coefficient. The feedback control system is actually PD controller, where $k_p = B_n/K_{en}\tau$ is proportional gain, $k_d = m_n/K_{en}\tau$ is differential gain.

It is noted that the above feedback controller has no ability to achieve favorable tracking. Therefore, a model-based feed-forward PID controller is designed to improve the tracking performance for the feedback control system.

$$C_{ff}(s) = \frac{1}{G_n(s)} = \frac{m_n}{K_{en}} s^2 + \frac{B_n}{K_{en}} s \tag{29}$$

where $k_{vff} = B_n/K_{en}$ is the velocity feedforward gain, $k_{aff} = m_n/K_{en}$ is the acceleration feedforward gain. After a simple deduction, at the time of nominal parameters are equal to the actual ones, the 2DoF-PID controller has the ability to track the reference instruction without any delay.

C. FRICTION FEEDFORWARD CONTROLLER

In a high precision motion system, the dynamic response can be affected to some extent by the nonlinear friction effects, which concretely express as existing a "dead zone" during passing through zero in the performance of velocity tracking. To solve this problem, a friction feedforward controller is adopted into the servo control system.

There is a number of theoretical models capable of representing pre-rolling friction behavior to some extent [38]. The

Lugre model, which is a bristle-inspired model and explains most of the observed phenomena, is shown as

$$
\begin{cases}
F_{fric} = \sigma_0 z + \sigma_1 \dot{z} + \alpha v \\
\dot{z} = v - \dfrac{\sigma_0 |v|}{g(v)} z \\
g(\dot{v}) = F_c + (F_s - F_c) e^{-\left(\frac{v}{v_s}\right)^2} + \alpha v
\end{cases}
\tag{30}
$$

where σ_0 and σ_1 are dynamic friction coefficients, F_c is the Coulomb friction, F_s is the maximum static friction, α is the viscous friction coefficient, v_s is the Stribeck velocity. Since the Lugre model is an implicit expression and the calculating step of the ODEs must be small enough otherwise falling in non-convergence, it is not suitable to be applied to a real-time servo algorithm. Hence, to modify the Lugre model to explicit, the friction model transfer to a two-stage model including pre-sliding and sliding regimes [31], [32]. However, these two-stage models depend on more parameters such as the parameters of each stage and a parameter for distinguish boundary, it is not practical to carry out a series of complex and accurate parameter identifications before setup the servo controller. Meanwhile, some friction models based on the neural network and fuzzy methods have been applied to estimate the friction in mechanical systems successfully [33], [34], however, its disadvantages such as the dependence on a super calculating capacity, a huge storage space, and a mass number of training samples limit its application in industry. Therefore, the classical Stribeck model mentioned in Eq. (4) can be introduced into a friction feedforward controller, which can be constructed as

$$
I_{fff} = \left(F_{cn} + (F_{sn} - F_{cn}) e^{-\left(\frac{v_d}{v_{sn}}\right)^2} \right) sign(v_d)
\tag{31}
$$

where I_{fff} is the output of friction feedforward controller, F_{cn} is the nominal Coulomb friction, F_{sn} is the maximum static friction, v_{sn} is the Stribeck velocity, v_d is the command velocity. These uncertain parameters of the Stribeck model can be identified by a set of constant acceleration experiments under ultra-low velocity conditions.

IV. SIMULATIONS AND EXPERIMENTAL RESULTS

A. EXPERIMENTAL SETUP

In order to verify the effectiveness of the proposed method, the experimental setup of the linear motor motion stage is shown in Fig. 6.

In this hardware configuration, an AKRIBIS iron-less PMLSM consisted of a set of winding coils (AUM4-S-S3-J-3.0) and a series of matched magnet tracks (AUM4-TL300) with a VAREDAN analog linear servo amplifier (LA-210) is applied to the servo system. The mover is supported by two THK rolling guides (LM-HSR-15A). The position feedback unit is a RENISHAW linear encoder, which is composed of a linear scale (RELM-380), a read head (SR-050A), and an interface box (SI-NN-0000). The servo controller is designed in the Power PMAC system, which can be viewed as an
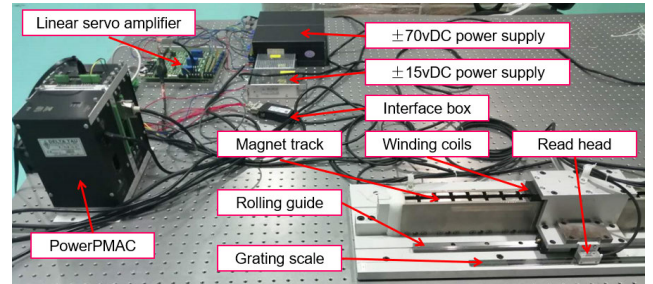

FIGURE 6. The experiment platform of the linear servo motor system.

TABLE 1. The main parameters of stage.

PMLSM	
Stroke	340(mm)
N-S poles pitch	30(mm)
Continuous power	73(W)
Continuous current	2.3Arms
Force constant	72(N/Arms)
Coil resistance	13.8(Ω)
Coil inductance	10.5(mH)
3-phase voltage	330(VDC)
Mass of winding coils	0.89(kg)
Linear Servo Amplifier	
Peak output current	10(Arms)
Continuous output current	2.5(Arms)
Motor bus voltage	±75(VDC)
Current loop bandwidth	Up to 10(kHz)
Command Signal (A and B inputs)	±10(V)
Power PMAC system	
Servo cycle period	0.4274211(ms)
Background cycle period	1(ms)
Feedback revolution	1.220703125(nm)

embedded computer with a hardware real-time operating system (RTOS). The main parameters of the motion stage are listed in Tab. 1.

It is worth noting that the analog linear amplifier is quite different from the common digital IGBT (or MOSFET) voltage-source-inverter controlled by SVPWM. That is a true Class AB linear output driver, whose features are low radiated noise and zero distortion of current. The linear amplifier is designed to accept two command signals (A and B) from a motor servo controller, and the command of the third phase $(C = -(A+B))$ is derived internally. At this point, the amplifier only offers the current loop control, the commutation has to be completed in the Power PMAC system. The position feedback is provided by the linear encoder, which is connected to the Power PMAC system directly.

B. MODEL IDENTIFICATION

Generally, in practice, it is hard to deduce the exact system parameters theoretically, the nominal values can only be obtained by system identification. A sinusoid chirp signal is selected in this section as the excitation source for the motion stage model identification, and the amplitude is maintained constant and the frequency increases linearly with time from 1 Hz to 30 Hz. The input of sources is the command current of
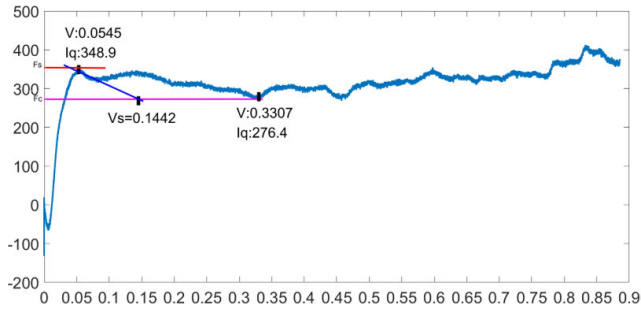
FIGURE 7. The constant acceleration experimental data and results.

FIGURE 8. The constant velocity experimental data and results.

PMLSM q axes, and the output of the stage is the actual position of the mover. Since the current loop control of bandwidth (up to 10 kHz) is far more than the maximum frequency of source input, the current loop transfer function can be directly viewed as "1".

The nominal model of the motion stage is identified by recursive least square method, denoted as Gn(s),

$$G_n(s) = \frac{0.05146s^2 + 30.58s + 52410}{s^2 + 4.191s + 0.1396} \quad (32)$$

It should be noted that the fitting probability of the identified results, which is just 74.35%, is not very well due to the existence of nonlinear friction factors in reciprocating movement and limitation of the working stroke.

The nonlinear friction phenomena mainly exist at the crossing zero-velocity zone, experimentation identified Stribeck parameters is designed as a constant accelerated movement with acceleration at 0.05 mm/s^2 from velocity zero, and records the actual velocity of the mover (v) and the command current (I_q). The results are drawn as Fig. 7.

The results of the friction coefficients identification are that the I_{sn} (equivalent current of the maximum static friction) is 348.9, the I_{cn} (equivalent current of the Coulomb friction) is 276.4, and the Stribeck velocity is 0.1442 mm/s.

In order to take the thrust ripple phenomenon into simulations, a constant velocity in 20 mm/s movement experiment is designed to determine the amplitude of thrust ripple in Eq. (3). In a constant velocity experiment [13], since the friction force does not change, the varying command current (I_q) is to be used to overcome the internal thrust fluctuation of the linear motor. Therefore, the amplitude value of I_q can represent the linear motor thrust ripple. The results are shown in Fig. 8.

The average of command current (I_q) for constant velocity movement is -157.415, and the amplitude of command current (I_q) is 157.415, then the A_r, according to Eq. (3), can be deduced to 0.006352.

C. SIMULATIONS
In order to validate the performance of the control strategy integrating the LESO and the FFF into a 2DoF-PID controller, the servo control system is simulated in MAT-LAB&SIMULINK. These simulations are carried out under
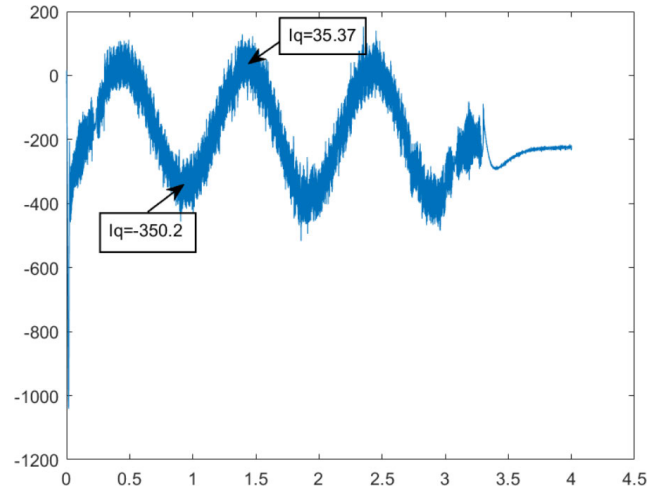
TABLE 2. The parameters of controller.

2DoF-PID	
τ	0.001
m	1
B	4.191
K_e	5.241×10^4
K_p	0.0799
K_d	0.0192
K_{vff}	7.99×10^{-5}
K_{aff}	1.91×10^{-5}
LESO	
ω	1000
h	4.274211×10^{-4}
FFF	
F_s	325.9
F_c	213.4
V_s	0.130

five controllers (PID, 2DOF-PID, PID-LESO, 2DOF-PID-LESO, and 2DOF-PID-LESO-FFF).

Remarkably, the parametric uncertainties will be considered in these simulations. Therefore, the parameters of the controller are designed according to the nominal model with a 25% deviation and the simulate plant is based on the exact value of the nominal model. The specific parameters of the controller are shown in Tab. 2.

The simulation results of the sinusoidal trajectory tracking without external working load are presented in Fig.9. In this simulation, the desired position signal is that a sinusoidal signal with an amplitude of 2 mm and a frequency of 5 Hz, and the disturbances include the end effects of PMLSM shown in Eq. (3) and the nonlinear friction of the rolling guide shown in Eq. (4). The parameters of these disturbance model are determined by a set of identification tests in the previous subsection.
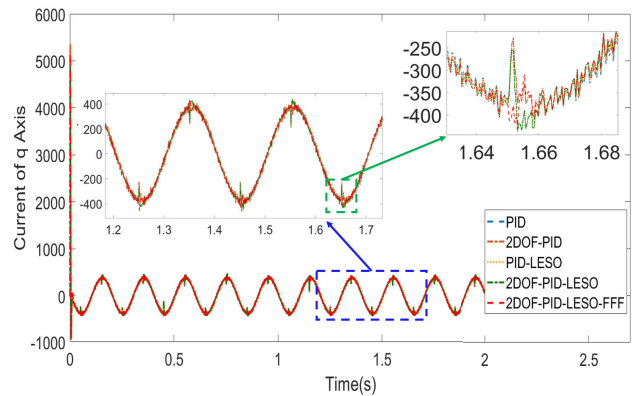
Under the sinusoidal command signal, the position responses under different methods and the simulative disturbances are shown in Fig. 9 (a), the tracking errors are shown in Fig. 9 (b), and the controller outputs are shown in Fig. 9 (c).
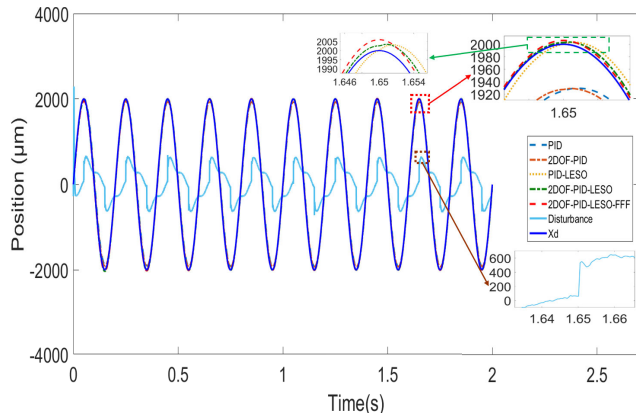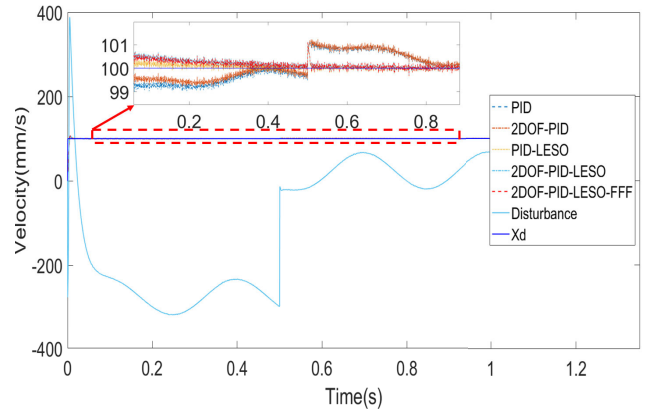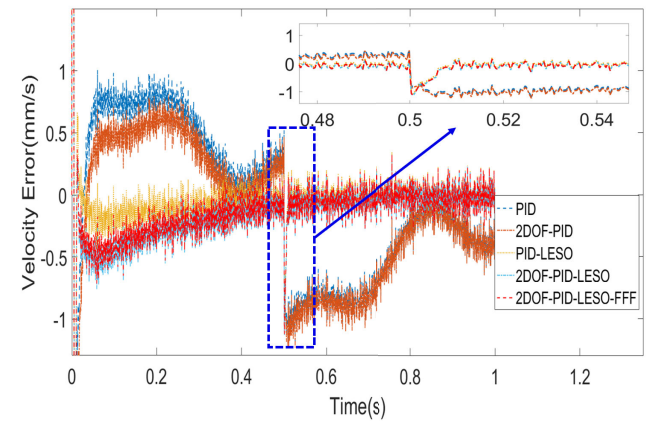
(a) The position response
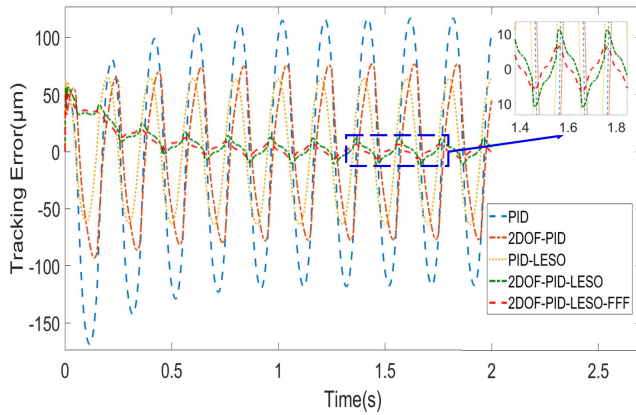
(b) Tracking errors

(c) Controller output

FIGURE 9. 2mm@5Hz sinusoidal trajectory tracking simulations.

(a) The velocity response

(b) Velocity errors

(c) Controller output

FIGURE 10. Constant motion at 100 *mm/s* with step disturbance simulations.
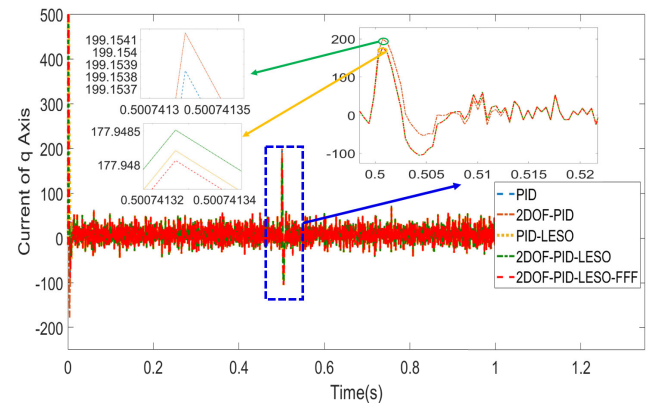
At the moment of 1.65 s, it can be an observer that the value of disturbance increases from 59 at 1.6501 s to 551 at 1.6509 s and then decreases to 474 at 1.6523 s. This abrupt change is due to the nonlinear friction happened on the speed close to the Stribeck velocity. The rest disturbance comes from PMLSM, in a small displacement reciprocating motion, the intensity of end effects is almost directly determined by the actual q axes current (i_q), and the period is nearly equal to the period of movement. At the same time, it is clear that the tracking performances of the PID-LESO and 2DoF-PID-LESO are obviously better than the PID and 2DoF-

PID respectively. Meanwhile, during the motion of 1.65 s, the tracking error of 2DoF-PID-LESO is no more than 11.5 μm. The tracking performance of 2DoF-PID-LESO-FFF is stable at around 6.6 μm, and its position response is almost no distortion during the peak and valley of sine.

Furthermore, the nominal parameter of m (in Eq. (26)) is uncertain because of the mass of clamp and workpiece mounted on the spindle is not fixed in practical use. Meanwhile, the viscous coefficient B will become bigger resulted

TABLE 3. Performance 2mm@5Hz sinusoidal signal with parametric uncertainties.

	$m = 1.2m_n$	$m = 1.4m_n$	$m = 1.6m_n$
PID	141.6 μm	170.5 μm	201.3 μm
2DoF-PID	78.8 μm	87.0 μm	94.3 μm
PID-LESO	64.0 μm	65.8 μm	65.8 μm
2DoF-PID-LESO	12.5 μm	13.5 μm	14.7 μm
2DoF-PID-LESO-FFF	7.6 μm	8.3 μm	9.1 μm
	$B = 2B_n$	$B = 4B_n$	$B = 6B_n$
PID	121.8 μm	137.1 μm	152.5 μm
2DoF-PID	83.0 μm	98.5 μm	113.1 μm
PID-LESO	64.5 μm	66.0 μm	67.5 μm
2DoF-PID-LESO	11.5 μm	12.2 μm	12.9 μm
2DoF-PID-LESO-FFF	7.1 μm	7.7 μm	8.2 μm

TABLE 4. The tracking errors of different methods.

	1 mm/s	10 mm/s	100 mm/s
PID	0.43 μm	2.21 μm	5.98 μm
2DoF-PID	0.23 μm	1.21 μm	2.58 μm
PID-LESO	0.31 μm	1.34 μm	1.80 μm
2DoF-PID-LESO	0.14 μm	1.05 μm	1.20 μm

from the oxidation of lubricating oil and the wear of the balls in the guides after long-term use. Hence, it is necessary to investigate the control ability of the above-mentioned five controllers in parametric uncertain conditions. Considering the setup of the servo controller is completed before ex-works delivery, therefore, the simulations have 6 types of uncertainties including $m = 1.2m_n$, $m = 1.4m_n$, $m = 1.6m_n$, $B = 2B_n$, $B = 4B_n$, $B = 6B_n$. The reference signal is the same as the Xd in Fig. 9 (a). To evaluate the control performance, the maximum tracking errors of controllers at the duration from 1.4s to 1.8s are applied as the assessment indicator. By comparing the simulation results in Tab. 3, the control performance of PID-LESO is the most stable (the maximum tracking errors is bounded between 64.0 μm and 67.5 μm) under different parameter uncertain conditions, it can be verified that the LESO as an adaptive observer can estimate and compensate the parametric uncertainties indeed. Since the performance of the general-purpose feedforward depends on an accurate model, the parametric-uncertainty influence ratio ($R_{pu} = \frac{max(maximum\ tracking\ errors)}{min(maximum\ tracking\ errors)}$-1) of 2DoF-PID-LESO-FFF, 2DoF-PID-LESO, and 2DoF-PID are 28.1%, 27.8%, and 43.5% respectively. The proposed method processes a certain robustness to face the parametric uncertainties.

The simulation results of the constant motion at 100 mm/s with a step external working load are presented in Fig. 10, and the disturbances include the end effects of PMLSM and working load. The step load is from 0 to 300 at 0.5 s.

Under the constant speed condition, the velocity responses under different methods and the simulative disturbances are illustrated in Fig. 10 (a), the velocity errors are illustrated in Fig. 10 (b), and the controller outputs are illustrated in Fig. 10 (c). It can be seen that the external work loading as an abrupt changing disturbance occurs at the 0.5 s, the velocity responses in the controllers of PID-LESO, 2DoF-PID-LESO, and 2DoF-PID-LESO-FFF can reach a steady state

(a) The position response

(b) Tracking errors
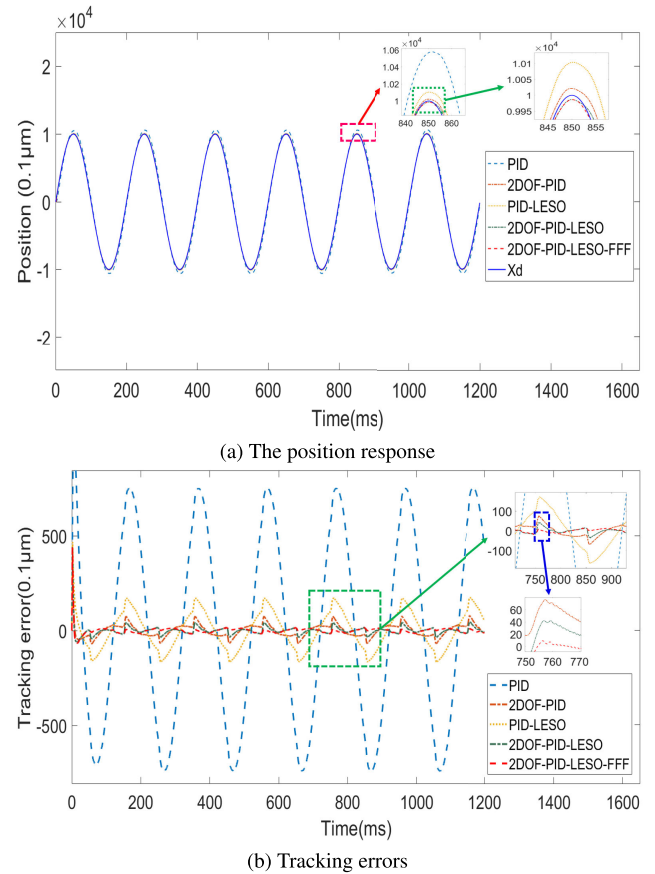
FIGURE 11. 2mm@5Hz sinusoidal trajectory tracking experiments.

less than 10 ms. However, the methods of PID and 2DoF-PID need as long as 0.32 s to the same state. This simulation is in a constant speed condition, the nonlinear friction effects barely exist. Therefore, the velocity error result of 2DoF-PID-LESO is nearly equal to 2DoF-PID-LESO-FFF. The maximum velocity error of PID-LESO in steady-state is 0.22 mm/s, and the ones of 2DoF-PID-LESO is even less than 0.15 mm/s. Meanwhile, the maximum velocity error of PID and 2DoF-PID are up to 0.40 mm/s. In summary, the LESO integrated into a servo controller can improve the disturbance rejection performance, and the FFF can eliminate the adverse effects of nonlinear friction to a certain extend. Meanwhile, the LESO can reduce the sensitivity of the general-purpose 2DoF-PID controller to the parametric uncertainties.

D. EXPERIMENTS

To verify the practicality of this method further, the proposed method is designed with model-blocks in SIMULINK, and then the model-blocks algorithm can be generated into C Code by the development kit of Power PMAC Target on MAT-LAB. The C code is compiled and downloaded into Power PMAC system by the Power PMAC Integrated Development Environment (IDE) software, and finally the compiled machine code runs at the Power PMAC's servo interrupt.
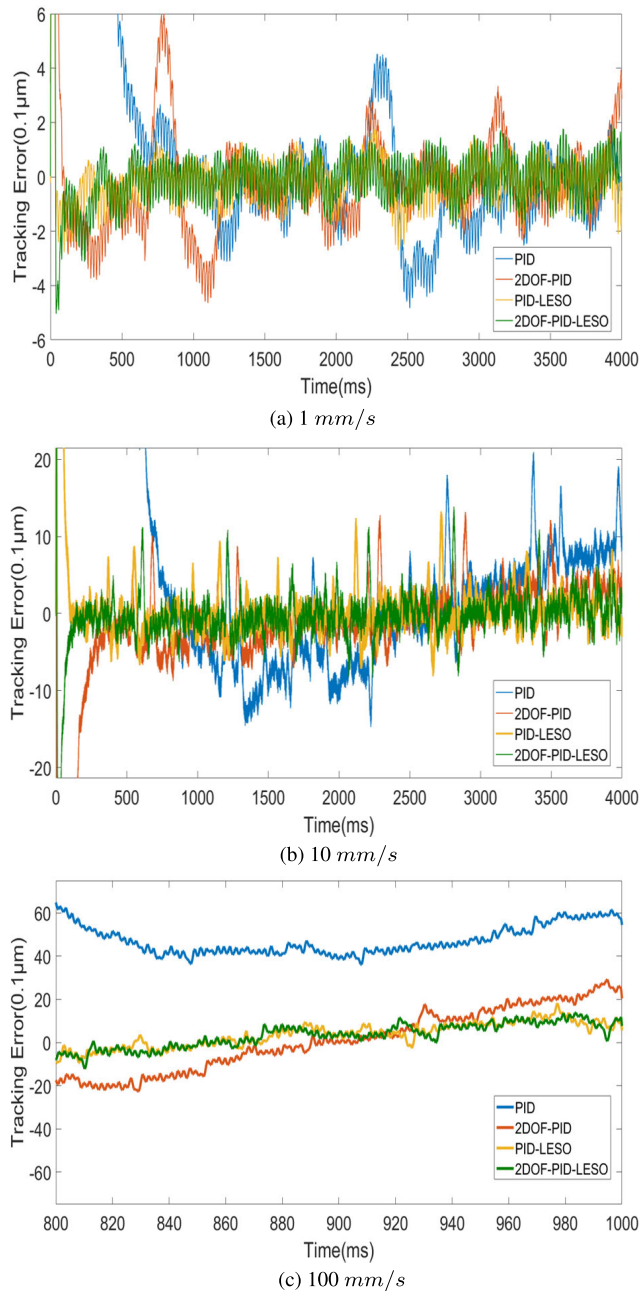
(a) 1 *mm/s*

(b) 10 *mm/s*

(c) 100 *mm/s*

FIGURE 12. The tracking errors of constant motion experiments.

On the stage mentioned in subsection 4.1, the position tracking experiments with a sinusoid reference signal were carried out under five methods (PID, 2DOF-PID, PID-LESO, 2DOF-PID-LESO, and 2DOF-PID-LESO-FFF). The sinusoidal signal is an amplitude of 1mm and a frequency of 5 Hz.

In this case, the position responses under different methods are shown in Fig. 11 (a), and the tracking errors are shown in Fig. 11 (b). It can be seen that the tracking error curves enter a stable tracking state after 20 ms. In the stable tracking state, the maximum tracking error of PID is up to 100 μm, and the PID controller integrated with a LESO can decrease the tracking error to 16.5 μm. Moreover, the tracking error

of the general-purpose 2DoF-PID is less than 7.7 μm, and the 2DoF-PID combined with a LESO can make tracking error down to 4.3 μm. Furthermore, the 2DoF-PID-LESO-FFF method proposed in this paper realizes the tracking error is no more than 1.5 μm.

To verify the stability of these methods, several whole-stroke constant velocity motion experiments were performed at different speeds (1 mm/s, 10 mm/s, and 100 mm/s). In the simulation results of Fig. 10, it can be seen that the FFF has little effects in a constant speed movement, therefore, the comparative experiments were carried out under four methods (PID, 2DOF-PID, PID-LESO, and 2DOF-PID-LESO). The results are shown in Fig.12.

In this condition, there is almost only one disturbance sourced from the end effects of PMLSM, and its intensity is determined by both the position of the mover and the actual q axes current (i_q). In the stable tracking state, the position tracking error of these control methods under different velocity conditions is summarized in Tab. 4.

Considering the results in Fig. 11 and Fig. 12, it is clear that the experimental results are consistent with the simulation, and the proposed method can be used to compensate both the slow-varying disturbances affected by thrust ripple and abrupt-changing interference caused by friction effectively. Finally, the tracking error of this method can be kept in the bounds of 1.5 μm under different conditions.

V. CONCLUSION

This paper presents the model of the three-phase iron-less PMLSM driving a linear positioning stage supported by rolling guides, and the stage is a prototype of the feeding system for a micro-precision turning machine tool. In this model, it contains the inherent force ripple of PMLSM and nonlinear friction force in rolling guides, the force ripple can be viewed as a slow-varying disturbance, and the nonlinear friction can be considered as an abrupt-changing interference. Since the machined surface quality (geometrical accuracy) is directly based on the tracking performance of the servo system, the control target is that the tracking errors no more than 3μm under extreme conditions. In order to perform this goal, a simple, effective and practical servo control method based on the common 2DoF-PID type controller integrated with the linear ESO and the FFF controller is presented. In this control framework, the 2DoF-PID is used to achieve a basic desired set-point tracking performance, the linear ESO is designed to compensate the slow-varying disturbances including thrust ripple of PMLSM, working load, and system parameter uncertainties, and the FFF controller based on Stribeck friction model is adopted to eliminate the nonlinear friction at the crossing zero-velocity zone for the rolling guides. Moreover, the system nominal parameters are obtained with a series of identification experiments and are used to design the servo controller. The simulations indicate that the proposed controller is effective, and the corresponding parameter tuning method is validated. Finally, the experimental results show

that the tracking error of the proposed method can be kept in the bounds of 1.5 μm.

REFERENCES

[1] M. Wang, L. Li, and D. Pan, "Detent force compensation for PMLSM systems based on structural design and control method combination," *IEEE Trans. Ind. Electron.*, vol. 62, no. 11, pp. 6845–6854, Nov. 2015.

[2] D.-J. Cheng, W.-S. Yang, J.-H. Park, T.-J. Park, S.-J. Kim, G.-H. Kim, and C.-H. Park, "Friction experiment of linear motion roller guide THK SRG25," *Int. J. Precis. Eng. Manuf.*, vol. 15, no. 3, pp. 545–551, Mar. 2014.

[3] R. Yang, M. Wang, L. Li, Y. Zenggu, and J. Jiang, "Integrated Uncertainty/Disturbance compensation with second-order sliding-mode observer for PMLSM-driven motion stage," *IEEE Trans. Power Electron.*, vol. 34, no. 3, pp. 2597–2607, Mar. 2019.

[4] B. Sencer and E. Shamoto, "Effective torque ripple compensation in feed drive systems based on the adaptive sliding-mode controller," *IEEE/ASME Trans. Mechatronics*, vol. 19, no. 6, pp. 1764–1772, Dec. 2014.

[5] S. Zhen, P. Chen, X. Chen, F. Qin, and H. Zhou, "Force ripple modeling and minimizing of an ironless permanent-magnet linear synchronous motor," *Int. J. Precis. Eng. Manuf.*, vol. 20, no. 6, pp. 927–935, Jun. 2019.

[6] M. Inoue and K. Sato, "An approach to a suitable stator length for minimizing the detent force of permanent magnet linear synchronous motors," *IEEE Trans. Magn.*, vol. 36, no. 4, pp. 1890–1893, Jul. 2000.

[7] S.-G. Lee, S.-A. Kim, S. Saha, Y.-W. Zhu, and Y.-H. Cho, "Optimal structure design for minimizing detent force of PMLSM for a ropeless elevator," *IEEE Trans. Magn.*, vol. 50, no. 1, pp. 1–4, Jan. 2014.

[8] Y.-W. Zhu, S.-G. Lee, K.-S. Chung, and Y.-H. Cho, "Investigation of auxiliary poles design criteria on reduction of end effect of detent force for PMLSM," *IEEE Trans. Magn.*, vol. 45, no. 6, pp. 2863–2866, Jun. 2009.

[9] Y.-W. Zhu, D.-H. Koo, and Y.-H. Cho, "Detent force minimization of permanent magnet linear synchronous motor by means of two different methods," *IEEE Trans. Magn.*, vol. 44, no. 11, pp. 4345–4348, Nov. 2008.

[10] S. Zhao and K. K. Tan, "Adaptive feedforward compensation of force ripples in linear motors," *Control Eng. Pract.*, vol. 13, no. 9, pp. 1081–1092, Sep. 2005.

[11] M.-T. Yan and Y.-J. Shiu, "Theory and application of a combined feedback–feedforward control and disturbance observer in linear motor drive wire-EDM machines," *Int. J. Mach. Tools Manuf.*, vol. 48, nos. 3–4, pp. 388–401, Mar. 2008.

[12] M.-T. Yan, K.-Y. Huang, Y.-J. Shiu, and Y. Chen, "Disturbance observer and adaptive controller design for a linear-motor-driven table system," *Int. J. Adv. Manuf. Technol.*, vol. 35, nos. 3–4, pp. 408–415, Dec. 2007.

[13] L. Bascetta, P. Rocco, and G. Magnani, "Force ripple compensation in linear motors based on closed-loop position-dependent identification," *IEEE/ASME Trans. Mechatronics*, vol. 15, no. 3, pp. 349–359, Jun. 2010.

[14] J. Xi, Z. Dong, P. Liu, and H. Ding, "Modeling and identification of iron-less PMLSM end effects for reducing ultra-low-velocity fluctuations of ultra-precision air bearing linear motion stage," *Precis. Eng.*, vol. 49, pp. 92–103, Jul. 2017.

[15] D. Zhang, Y. Chen, W. Ai, and Z. Zhou, "Precision motion control of permanent magnet linear motors," *Int. J. Adv. Manuf. Technol.*, vol. 35, nos. 3–4, pp. 301–308, Dec. 2007.

[16] Y. Wang, H. Yu, Z. Che, Y. Wang, and C. Zeng, "Extended state observer-based predictive speed control for permanent magnet linear synchronous motor," *Processes*, vol. 7, no. 9, p. 618, 2019.

[17] H.-Y. Jin and X.-M. Zhao, "Extended Kalman filter-based disturbance feed-forward compensation considering varying mass in high-speed permanent magnet linear synchronous motor," *Electr. Eng.*, vol. 101, no. 2, pp. 537–544, Jun. 2019.

[18] R. Yang, L.-Y. Li, M.-Y. Wang, C.-M. Zhang, and Y.-M. Zeng-Gu, "Force ripple estimation and compensation of PMLSM with incremental extended state modeling-based Kalman filter: A practical tuning method," *IEEE Access*, vol. 7, pp. 108331–108342, 2019.

[19] S.-L. Chen and T.-H. Hsieh, "Repetitive control design and implementation for linear motor machine tool," *Int. J. Mach. Tools Manuf.*, vol. 47, nos. 12–13, pp. 1807–1816, Oct. 2007.

[20] Y. Luo, Y. Chen, and Y. Pi, "Cogging effect minimization in PMSM position servo system using dual high-order periodic adaptive learning compensation," *ISA Trans.*, vol. 49, no. 4, pp. 479–488, Oct. 2010.

[21] K. Cho, J. Kim, S. B. Choi, and S. Oh, "A high-precision motion control based on a periodic adaptive disturbance observer in a PMLSM," *IEEE/ASME Trans. Mechatronics*, vol. 20, no. 5, pp. 2158–2171, Oct. 2015.

[22] K. Cho and K. Nam, "Periodic learning disturbance observer based precision motion control in PMLSM motion systems considering long-term instability problem," *Int. J. Precis. Eng. Manuf.*, vol. 17, no. 9, pp. 1101–1112, Sep. 2016.

[23] W. Zhang, N. Nan, Y. Yang, W. Zhong, and Y. Chen, "Force ripple compensation in a PMLSM position servo system using periodic adaptive learning control," *ISA Trans.*, vol. 95, pp. 266–277, Dec. 2019, doi: 10.1016/j.isatra.2019.04.032.

[24] X. Fu, X. Yang, and Z. Chen, "A new linear motor force ripple compensation method based on inverse model iterative learning and robust disturbance observer," *Complexity*, vol. 2018, pp. 1–19, Dec. 2018.

[25] M. A. M. Cheema, J. E. Fletcher, M. Farshadnia, and M. F. Rahman, "Sliding mode based combined speed and direct thrust force control of linear permanent magnet synchronous motors with first-order plus integral sliding condition," *IEEE Trans. Power Electron.*, vol. 34, no. 3, pp. 2526–2538, Mar. 2019.

[26] X. Zhao and D. Fu, "Adaptive neural network nonsingular fast terminal sliding mode control for permanent magnet linear synchronous motor," *IEEE Access*, vol. 7, pp. 180361–180372, 2019.

[27] D. Jiang, W. Yu, J. Wang, Y. Zhao, Y. Li, and Y. Lu, "A speed disturbance control method based on sliding mode control of permanent magnet synchronous linear motor," *IEEE Access*, vol. 7, pp. 82424–82433, 2019.

[28] D. P. Yu, G. S. Hong, and Y. S. Wong, "Profile error compensation in fast tool servo diamond turning of micro-structured surfaces," *Int. J. Mach. Tools Manuf.*, vol. 52, no. 1, pp. 13–23, Jan. 2012.

[29] X. D. Zhang, F. Z. Fang, Q. Q. Wu, X. L. Liu, and H. M. Gao, "Coordinate transformation machining of off-axis aspheric mirrors," *Int. J. Adv. Manuf. Technol.*, vol. 67, nos. 9–12, pp. 2217–2224, Aug. 2013.

[30] X.-C. Xi, A.-N. Poo, and G.-S. Hong, "Tracking error-based static friction compensation for a bi-axial CNC machine," *Precis. Eng.*, vol. 34, no. 3, pp. 480–488, Jul. 2010.

[31] M. Ruderman, "Tracking control of motor drives using feedforward friction observer," *IEEE Trans. Ind. Electron.*, vol. 61, no. 7, pp. 3727–3735, Jul. 2014.

[32] M. Yang, J. Yang, and H. Ding, "A two-stage friction model and its application in tracking error pre-compensation of CNC machine tools," *Precis. Eng.*, vol. 51, pp. 426–436, Jan. 2018.

[33] M. Sparham, A. A. D. Sarhan, N. A. Mardi, M. Hamdi, and M. Dahari, "ANFIS modeling to predict the friction forces in CNC guideways and servomotor currents in the feed drive system to be employed in lubrication control system," *J. Manuf. Processes*, vol. 28, pp. 168–185, Aug. 2017.

[34] Z. Ben Hazem, M. J. Fotuhi, and Z. Bingul, "A comparative study of the joint neuro-fuzzy friction models for a triple link rotary inverted pendulum," *IEEE Access*, vol. 8, pp. 49066–49078, 2020.

[35] J. Han, "From PID to active disturbance rejection control," *IEEE Trans. Ind. Electron.*, vol. 56, no. 3, pp. 900–906, Mar. 2009.

[36] P. Li and G. Zhu, "IMC-based PID control of servo motors with extended state observer," *Mechatronics*, vol. 62, Oct. 2019, Art. no. 102252.

[37] S. Shao and Z. Gao, "On the conditions of exponential stability in active disturbance rejection control based on singular perturbation analysis," *Int. J. Control*, vol. 90, no. 10, pp. 2085–2097, Oct. 2017.

[38] F. J. Villegas, R. L. Hecker, M. E. Peña, D. A. Vicente, and G. M. Flores, "Modeling of a linear motor feed drive including pre-rolling friction and aperiodic cogging and ripple," *Int. J. Adv. Manuf. Technol.*, vol. 73, nos. 1–4, pp. 267–277, Jul. 2014.

XIUFENG LIU was born in Hubei, China. He received the B.E. degree in electronic information science and technology from China Three Gorges University (CTGU), Yichang, China, in 2011, and the M.S. degree in mechanical engineering from the Wuhan University of Science and Technology (WUST), Wuhan, in 2015. He is currently pursuing the Ph.D. degree with the School of Mechanical Science and Engineering, Huazhong University of Science and Technology. His current research interests include motor servo control, CNC technology, and ultraprecision machine tools.

HAIYIN CAO was born in Henan, China. He received the B.E. degree in mechanical design, manufacturing and automation from the Huazhong University of Science and Technology, Wuhan, China, in 2011, where he is currently pursuing the Ph.D. degree with the School of Mechanical Science and Engineering. His current research interests include hydrostatic/hybrid bearings and ultraprecision machine tools.

WEI WEI was born in Rugao, Jiangsu, China, in 1987. He received the M.S. and Ph.D. degrees in mechatronics engineering from the Harbin Institute of Technology, Harbin, China, in 2010 and 2015, respectively. He is currently an Engineer at the Institute of Machinery Manufacturing Technology, China Academy of Engineering Physics. His research interests are motor control, hydraulic system control, robot control, and machinery dynamics. In these areas, he has authored or coauthored more than 15 technical articles, one textbook, and holds five patents.

JINZHOU WU received the B.E. degree in mechanical design manufacturing and automation from Central South University, Hunan, China, in 2018. He is currently pursuing the M.S. degree with the School of Mechanical Science and Engineering, Huazhong University of Science and Technology. His current research interest is servo control of ultraprecision CNC machine tool.

BO LI was born in Longchang, Sichuan, China, in 1977. He received the Ph.D. degree from the Huazhong University of Science and Technology, Wuhan, China. His research interest is mainly in the area of manufacturing informatization and digital equipment. He has published more than ten research articles in scholarly journals concerning the above research areas and participated in a couple of academic conferences and seminars.

YU HUANG was born in Longsheng, Guangxi, China, in 1972. He received the Ph.D. degree from the School of Mechanical Science and Engineering, Huazhong University of Science and Technology, Wuhan, China. He is currently a Professor and a Ph.D. Supervisor at the School of Mechanical Science and Engineering, Huazhong University of Science and Technology. His research interests are hydrostatic/hybrid bearings, laser fine processing technology and equipment, and high power laser cutting and welding equipment.

. . .